# Regularities of Structural Rearrangements in Single- and Bicrystals Near the Contact Zone


**Konstantin P. Zolnikov, Dmitrij S. Kryzhevich, and Aleksandr V. Korchuganov**

**Abstract** The chapter is devoted to the analysis of the features of local structural rearrangements in nanostructured materials under shear loading and nanoindentation. The study was carried out using molecular dynamics-based computer simulation. In particular, we investigated the features of symmetric tilt grain boundary migration in bcc and fcc metals under shear loading. The main emphasis was on identifying atomic mechanisms responsible for the migration of symmetric tilt grain boundaries. We revealed that grain boundaries of this type can move with abnormally high velocities up to several hundred meters per second. The grain boundary velocity depends on the shear rate and grain boundary structure. It is important to note that the migration of grain boundary does not lead to the formation of structural defects. We showed that grain boundary moves in a pronounced jump-like manner as a result of a certain sequence of self-consistent displacements of grain boundary atomic planes and adjacent planes. The number of atomic planes involved in the migration process depends on the structure of the grain boundary. In the case of bcc vanadium, five planes participate in the migration of the $\Sigma5(210)[001]$ grain boundary, and three planes determine the $\Sigma5(310)[001]$ grain boundary motion. The $\Sigma5(310)[001]$ grain boundary in fcc nickel moves as a result of rearrangements of six atomic planes. The stacking order of atomic planes participating in the grain boundary migration can change. A jump-like manner of grain boundary motion may be divided into two stages. The first stage is a long time interval of stress increase during shear loading. The grain boundary is motionless during this period and accumulates elastic strain energy. This is followed by the stage of jump-like grain boundary motion, which results in rapid stress drop. The related study was focused on understanding the atomic rearrangements responsible for the nucleation of plasticity near different crystallographic surfaces of fcc and bcc metals under nanoindentation. We showed that a wedge-shaped region, which consists of atoms with a changed symmetry of the nearest environment, is formed under the indentation of the (001) surface of the copper crystallite. Stacking faults arise in the (111) atomic planes of the contact zone under the indentation of the (011)

K. P. Zolnikov (✉) · D. S. Kryzhevich · A. V. Korchuganov
Institute of Strength Physics and Materials Science of Siberian Branch of the Russian Academy of Sciences, 2/4 Akademicheskii Ave, Tomsk 634055, Russia
e-mail: kost@ispms.ru



G.-P. Ostermeyer et al. (eds.), *Multiscale Biomechanics and Tribology of Inorganic and Organic Systems*, Springer Tracts in Mechanical Engineering,
https://doi.org/10.1007/978-3-030-60124-9_14

surface. Their escape on the side free surface leads to a step formation. Indentation of the (111) surface is accompanied by nucleation of partial dislocations in the contact zone subsequent formation of nanotwins. The results of the nanoindentation of bcc iron bicrystal show that the grain boundary prevents the propagation of structural defects nucleated in the contact zone into the neighboring grain.

**Keywords** Nanocrystalline materials · Plastic deformation · Grain boundary migration · Atomic displacements · Structural defects · Shear loading · Nanoindentation · Molecular dynamics

## 1 Introduction

The behavior of the material in contact zones is a complex multiscale process [1], which depends on a number of parameters: the roughness of the contacting surfaces, the chemical composition of materials, loading parameters, etc. [2]. The features of fracture and wear processes in the surface layer of the materials during friction are largely determined by the shear stresses. Note that the nucleation of structural changes in materials always begins at the atomic scale. Moreover, the features of the internal structure of the material, in particular, the grain boundaries (GB), can have a significant effect on structural changes in the contact zone [3, 4]. The role of GBs in the processes of friction and wear is most significant for nanostructured metallic materials having a high GB density [5]. Note that large interest in such materials is due to their high operational properties and therefore broad prospects for their use in mechanical engineering, technology, medicine, as well as in the creation of structures for various purposes. Nanostructured metallic materials have high strength at low temperatures due to GB hardening (Hall-Petch effect). At the same time, they become superplastic at high temperatures due to GB softening, which facilitates and improves their treatment in different technological processes.

Dislocation glide is substantially suppressed in nanostructured materials [6–8]. Furthermore, the role of different modes of GB deformation or twinning is enhanced [9–12]. The main mechanism of GB deformation becomes intergranular sliding, which largely determines superplastic deformation. The experimental data and the results of computer simulations confirm the significant contribution of intergranular sliding to the plastic behavior of nanostructured metallic materials under high strain-rate loading, which lead to the formation of high local stresses [13].

GB sliding leads to the nucleation of various defects in triple junctions. These defects become sources of internal stresses and can lead to crack nucleation and brittle fracture of the material [14, 15]. The physical nature and dynamics of accommodation processes in nanostructured materials under mechanical loading are extensively studied in materials science. Typical examples of accommodation mechanisms include the emission of lattice dislocations from the zone of triple junctions, diffusion processes, rotational deformation, splitting, and migration of GBs [16]. At that, GB

migration and splitting caused by GB sliding are often realized in the form of collective self-consistent displacement of atoms in the interface region, which significantly enhances the efficiency of material accommodation on the applied loading.

A significant part of the studies on the atomic mechanisms of friction, wear, and plasticity in nanocrystalline materials is carried out using various computer simulation approaches. Still many issues related to the nucleation and development of plastic deformation, structural transformations, and wear in the contact zones in nanostructured metallic materials remain debatable. This is due to both the great variety of chemical composition and internal structure of nanostructured materials, and the difficulties in their experimental studying at the microscopic level, associated with small spatial and temporal intervals of the processes.

The considerable interest in the study of the tribological properties of nanostructured metallic materials is the elucidation of structural transformations in bicrystals with different types of GBs under mechanical loading. In [17] it was shown that some types of GBs in fcc materials can migrate with abnormally high speeds under shear loading. This can lead to a change in the structure and tribological parameters of the material in the friction zone. Therefore, the identification of mechanisms responsible for GB migration is important for the development of new approaches to stabilize the internal structure of materials in the friction zone.

The results of molecular dynamics simulation showed that the GB migration along the normal often occurs together with the tangential displacement of the grains, which leads to the shear deformation of the lattice intersected by the GB [18]. In turn, the shear stresses applied to the GB can cause its normal displacement, i.e. during GB migration, one grain will grow at the expense of another. Depending on the direction of the applied shear stresses, the GB can shift either in one direction or in the opposite direction along the normal vector.

High-rate shear loading of the crystallite can lead to the formation of vortex motion of atoms in the region of symmetric tilt GBs [19, 20]. The dimensions of the vortices in diameter are several lattice parameters and are characterized by significant atomic displacements not only in the direction of loading, but also in the GB plane. This process is dynamic, and the accommodation of the material is carried out on the basis of an abnormally high GB velocity. GB migration is based on self-consistent collective atomic displacements. Despite the fact that the displacement of each individual atom in the GB region is small, self-consistent vortex atomic displacements result in reconstruction of a significant region of one grain into the structure of the neighboring grain.

In this chapter, the regularities of structural rearrangements in the region of symmetric tilt GBs in bcc vanadium and fcc nickel initiated by high-speed shear loading are considered. Features of the behavior of materials during contact interaction are presented by studying atomic mechanisms of nucleation and development of plasticity in fcc copper and bcc vanadium metals with an ideal structure and GBs under nanoindentation.

## 2 Materials and Methods

Studies were carried out on the base of the molecular dynamics method using the LAMMPS software package [21]. The interatomic interaction in bcc vanadium and iron was described using many-body potentials [22, 23] calculated with the embedded atom method in the Finis-Sinclair approximation. In the case of fcc nickel and copper, the interatomic interaction was described using many-body potentials [24, 25]. Parallelepiped-shaped samples were modeled. The gamma-surface minimization algorithm [26] was used to construct GBs. Visualization of the simulation results was carried out using the OVITO package [27].

We used two parameters to identify the atoms involved in the generation of structural changes, the reduced slip vector [28] and the topological parameter that takes into account the nature of the relative positions of the nearest neighbors for each atom (common neighbor analysis) [29]. The reduced slip vector $P_i$ is a dimensionless quantity, which is determined by the formula: where $j$ is the nearest neighbor of atom $i$, $N_s$ is the number of neighboring atoms, $\bar{r}^{ij}$ and $\bar{r}_0^{ij}$ are the vectors between the positions of atoms $i$ and $j$ in the current and initial positions, respectively.

$$P_i = \frac{1}{N_S} \sum_{i \neq j} \frac{\left(\bar{r}^{ij} - \bar{r}_0^{ij}\right)}{\left|\bar{r}_0^{ij}\right|},$$

## 3 Features of Symmetric Tilt Grain Boundary Migration in Metals

The objects of the study were vanadium bicrystals containing about 40, 000 atoms. Periodic boundary conditions were simulated in the $X$ and $Z$ directions, rigid boundary conditions were set in the $Y$ direction (Fig. 1). The initial temperature

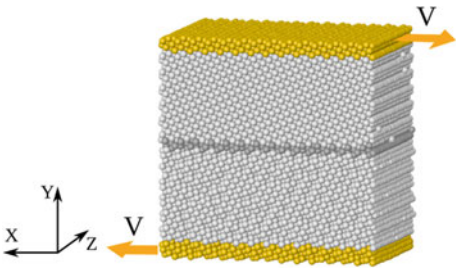


**Fig. 1** The initial structure and the loading scheme of the sample containing the Σ5(210)[001] GB, and the loading scheme. The grips are marked in yellow, the GB region is highlighted in gray, directions of the grip shift are indicated by arrows

of the samples was 300 K. The calculations were performed for samples containing two types of symmetric tilt GBs: Σ5 (310) [001] and Σ5 (210) [001]. The shear loading rate in the *X* direction in different calculations varied from 1 to 100 m/s.

The simulation results showed that shear loading of bicrystals leads to a high-speed GB migration. We found that the velocity of GB motion is determined by the shear rate and the GB structure. The GB velocity increases with an increase in the shear rate. The average velocity of the Σ5 (210) [001] GB for the considered shear rates is within the range from 3 to 280 m/s. The average velocity in the case of the Σ5 (310) [001] GB is significantly lower and is in the range from 2 to 180 m/s. It is important to note that plasticity does not nucleate in the samples despite the high GB migration velocity.

During the loading, a periodic increase and drop of stresses occur. The GB migrates in a pronounced jump-like manner due to the crystallinity of the sample. Upon stress drop, the instant GB migration velocity rapidly increases, reaches a maximum value, and drops to almost zero. This is clearly seen from a comparison of the corresponding curves in Fig. 2. Note that the dependence of stresses on time in the interval of growth and drop is linear. This indicates that no structural defects are generated in the loaded sample.

Simulation results showed that atomic rearrangements in the Σ5 (310) [001] and Σ5 (210) [001] GB regions responsible for GB migration are significantly different. The displacement of the Σ5 (210) [001] GB is a result of atomic rearrangements in three atomic planes: two planes of the GB and the adjacent upper grain plane. Green color shows atomic planes belonging to the GB, and blue shows the plane of the upper grain in Fig. 3 This plane adjusts to the structure of the lower grain

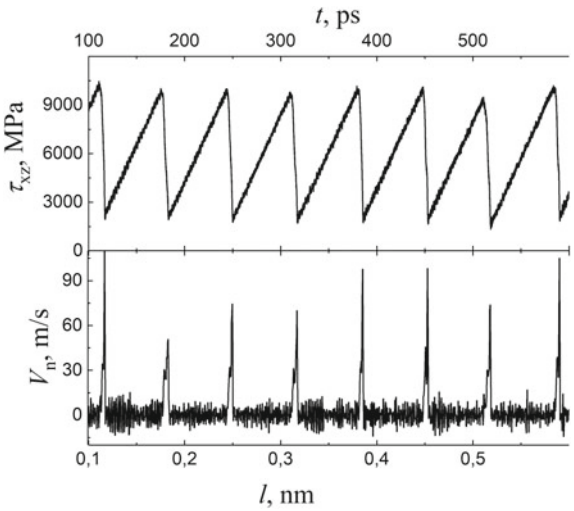


**Fig. 2** The velocity of the Σ5 (210) [001] GB migration in the normal direction ($V_n$), and stress $\tau_{xz}$ depending on the grip displacement. Shear rate is 1 m/s

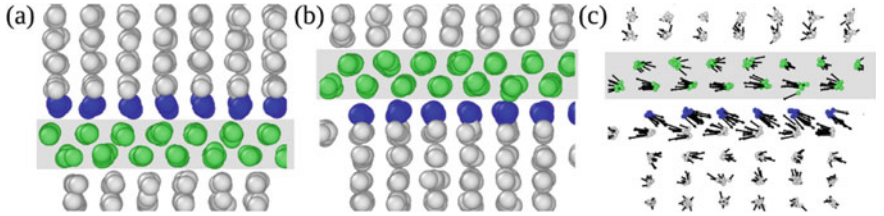


**Fig. 3** Fragment of the sample with the Σ5 (310) [001] GB before loading (**a**) and after the GB displacement on three interplanar distances (**b**). The projection of the displacements on the *YZ* plane (**c**). The shear rate is 1 m/s. The GB region is marked with gray

during shear loading (Fig. 3b). The resulting atomic displacements in the YZ plane after such a rearrangement are shown in Fig. 3c. The value of these displacements is about 0.08 nm. Analysis of simulation results showed that the incorporation of the atomic plane of the upper grain into the structure of the lower grain is realized as a sequence of three successive displacements in different directions. The duration of each displacement for the grip velocity of 1 m/s is about 3.6 ps. The values of these three displacements are approximately equal to 0.07, 0.03, and 0.06 nm. As a result of such displacements, the atoms of the blue plane successively occupy the positions of the atoms of the upper and then the lower GB planes and, finally, adjust to the lattice of the lower grain.

Three atomic planes are simultaneously involved in the displacement of the Σ5 (210)[001] GB. The four atomic planes make up the GB (highlighted in gray), and the three atomic planes (highlighted in blue, green, and red) belong to the upper grain in Fig. 4. As a result of a certain sequence of displacements the upper grain planes first rearranged into the structure of GB planes and then adjust to the structure of the lower grain. The value of the resulting displacements of the atoms of the blue plane during its transformation to the lower grain is 0.05 nm. During this interval, two jump-like displacements occur, each with a duration of 4.0 ps. The value of the first displacement is 0.04 nm, the second is 0.05 nm. After the first displacement, the

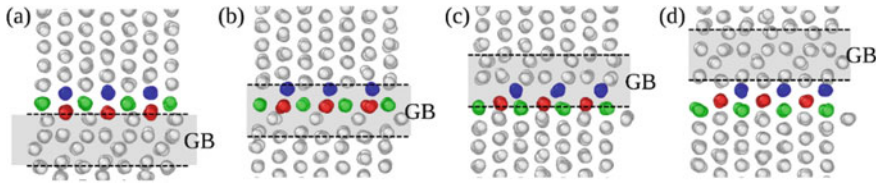


**Fig. 4** Fragment of the structure with the Σ5 (210)[001] GB before loading (**a**), structural configuration of colored planes after first (**b**) and second (**c**) GB displacement, and after the GB was displaced on four interplanar distances (**d**). The GB region is located between the dashed lines and is highlighted in gray. The shear rate is 1 m/s

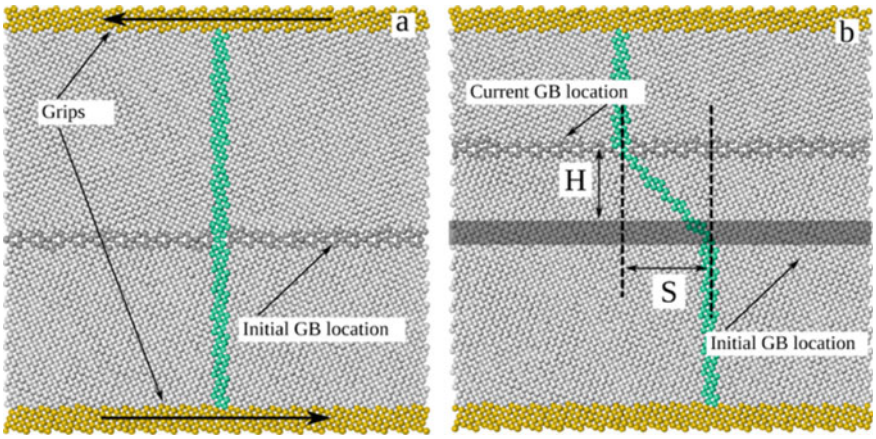


**Fig. 5** Crystallite structure and the GB position at different points in time after the start of loading: 0 ps (**a**); 300 ps (**b**). Arrows in **a** show the displacement direction of the grips. The green line shows the position of the atoms forming a vertical line along the middle of the sample before loading

selected planes are rearranged into the GB structure (Fig. 4b). The second displacement changes the stacking order of green and red planes and then adjusts the green plane to the lower grain (Fig. 4c, d).

Note that the atomic planes far from the GB also have a pronounced periodicity of motion in the normal direction. It is due to the crystallinity of the sample structure and the constant velocity of the grips. However, the jump-like motion of these planes is less pronounced in comparison with atomic planes belonging to GB.

The structural transformations leading to high-speed migration of GBs in fcc metals under shear loading were studied for nickel bicrystals containing the Σ5 (310)[001] symmetric tilt GB. The simulated sample was composed of about 70,000 atoms. Periodic boundary conditions were simulated in directions parallel to GB, and rigid boundary conditions were set in the third one. The loading scheme and the position of the GB are shown in Fig. 5a. The initial temperature of the sample was 300 K. The shear loading rate in different simulations varied from 1 to 100 m/s.

The simulation results showed that shear loading of nickel sample causes a high-speed GB motion along the normal to its plane. To analyze the peculiarities of the GB motion in the bicrystal, a vertical layer was selected with a thickness of several lattice parameters normal to the GB plane. It was found that the atoms of this layer in the interval between the initial and final positions of the GBs have a pronounced displacement gradient (Fig. 5b). Atoms outside this interval are displaced by equal distances with grips. This is a shear-induced displacement of the GB. Such character of the GB displacement was revealed experimentally in [30]. It is one of the main mechanisms of grain growth and is quite common in the processes of recrystallization of the structure. For a quantitative description of this GB displacement, a coupling factor is introduced. It is defined as the ratio of the lateral ($S$) and normal ($H$) displacement values:

$$b = S/H.$$

The coupling factor depends on the structure of the GB region and the sample temperature [18]. For simulated GB, the coefficient $b$ is approximately equal to 1.

The change in the shear stress $\tau_{xy}$ during the GB motion is shown in Fig. 6. One can see that the GB moves in a jump-like manner, which is due to the sawtooth nature of the change in shear stress. Note that the segments of the curve on which the shear stress increases correspond to the flat segments on the GB displacement curve. The segments of the $\tau_{xy}$ curve at which the drop occurs correspond to the GB displacement. The pronounced periodicity of the curves in Fig. 6 is associated with the discreteness of the crystallite structure and the symmetry of the GB. At the same time, thermal fluctuations of the atomic system cause deviations from this periodicity.

Analysis of the simulation results showed that the GB motion is realized through a certain sequence of transformations of typical structural elements in the intergranular region. Figure 7 shows a fragment of the structure in the GB region at different points in time. This fragment contains two atomic planes along the normal to the plane of the figure. The Roman numerals denote the atoms in the GB region, which belonged to the upper grain at the initial moment. Note that the atoms with numbers I and III belong to the same plane in the normal direction to the figure, and II and IV belong to the other plane. We revealed that the transformation of the GB atomic layer of the upper grain into the structure of the lower grain occurs through three characteristic jump-like displacements of numbered atoms in the $XY$ plane. The directions and values of these three displacements for numbered atoms are shown in Table 1. The GB motion in the lateral and normal direction to its plane during loading is always provided by the indicated displacements of the boundary atoms.

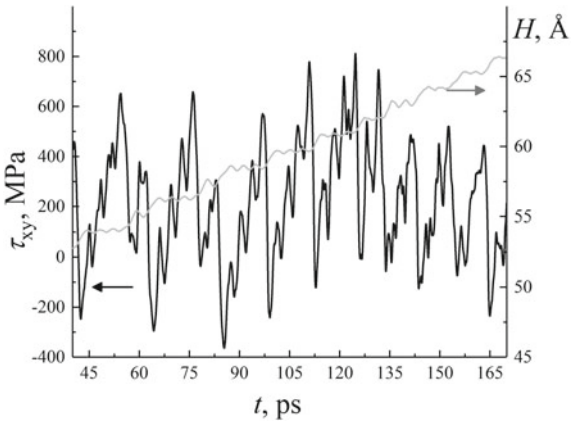


**Fig. 6** Dependence of the shear stress and coordinates of the Σ5 (310)[001] GB position in nickel bicrystal on time. The black curve is shear stress; the gray curve is the GB position

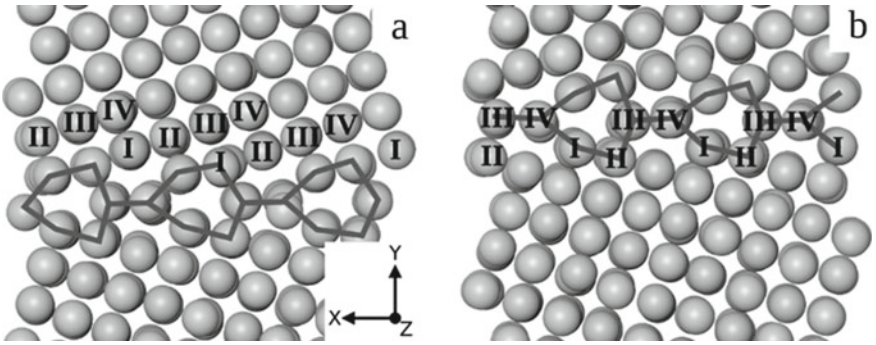


**Fig. 7** Fragment of the structure containing the Σ5 (310)[001] GB in nickel at the following points in time after the start of the shear: **a** 22.5 ps; **b** 43 ps. Lines indicate the GB structural elements

**Table 1** Atomic displacements providing GB motion under shear loading

| Atom numbers | First displacement, Å (X; Y) | Second displacement, Å (X; Y) | Third displacement, Å (X; Y) |
|---|---|---|---|
| I | (0.7; 0.1) | (0.4; 0.0) | (−0.5; 0.0) |
| II | (0.6; 0.0) | (0.3; −0.5) | (−0.4; −0.4) |
| III | (0.5; 0.0) | (0.5; 0.1) | (0.6; 0.0) |
| IV | (0.6; 0.0) | (0.4; 0.0) | (0.4; −0.4) |

Note that the motion of the symmetric tilt GB is realized without nucleation of structural defects. The use of periodic boundary conditions does not allow grain rotation during the displacement process. Since a tilt symmetric boundary is simulated, both grains have the same shear moduli in the direction of applied loading. Therefore, the GB motion is completely due to the coupling effect.

## 4 Peculiarities of Plasticity Nucleation in Metals Under Nanoindentation

One of the most informative and effective methods for studying the physical and mechanical properties of materials during contact interaction is nanoindentation. A change in the indentation conditions allows a systematic study of the influence of various factors on the processes occurring in the contact zones of the materials. As a rule, the aim of works related to computer simulation of the material behavior under indentation is to study the mechanisms of plastic deformation in the zone of a spherical or pyramidal indenter, visualize defect structures, and interpret load-indentation curves [31–34]. Despite the high information content of such studies, it is difficult to analyze the results due to the complex deformation pattern. For the

clearer and simpler interpretation of the indentation results, it is convenient to use an extended indenter of a cylindrical shape [35–37]. For this choice of the indenter, the contact region is linearly extended from one face of the sample to the other. The loading scheme of a copper crystallite with such an indenter is shown in Fig. 8. The axis of the indenter was parallel to the loaded crystallite surface. Free boundary conditions were set along this axis. The loaded face was a free surface, while atomic positions of several layers of the opposite face were fixed in the indentation direction. The lateral faces of crystallites were simulated as free surfaces. The indentation rate was 25 m/s. The simulated crystallites were loaded at 300 K.

To study the behavior of simulated crystallite under indentation the loading force was calculated as a function of the indentation depth. The loading force ($F$) was defined as the total force acting on the indenter from the loaded crystallite. The indentation depth ($d$) was calculated as the distance from the lower boundary of the indenter surface to the level of the crystallite surface in the initial state. The results of the calculation of the loading force - indentation depth dependence are shown in Fig. 9.

The indenter and crystallite begin to interact as soon as the distance between them becomes smaller than the cutoff radius of the interatomic interaction. Initially, an attractive force arises between the indenter and the loaded surface (this corresponds to a negative value of the loading force in Fig. 9). This effect is called "jump-to-contact" [38]. During the indenter displacement, the attractive force changes into repulsive. In accordance with this, the loading force in Fig. 9 has a pronounced minimum. The dependence of the indentation force on the indentation depth can be divided into four stages. The first stage is characterized by a linear dependence of the loading force on the indentation depth and corresponds to the elastic response of the material. At the beginning of the second stage, local structural transformations are generated in the contact zone (Fig. 10a). The generation of such local structural transformations

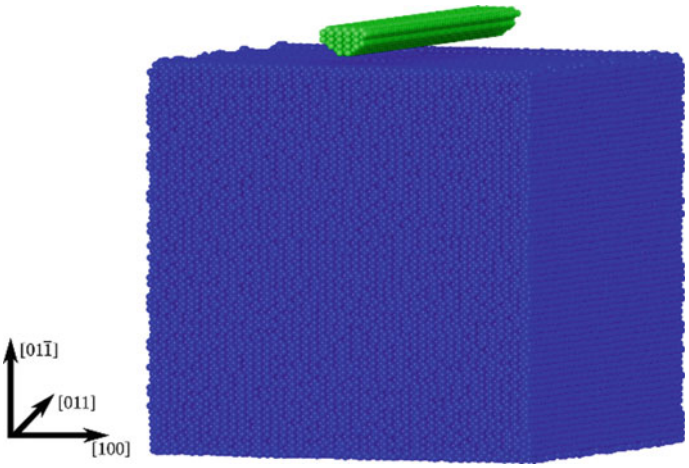


**Fig. 8** Indentation scheme and crystallographic orientation of the simulated system

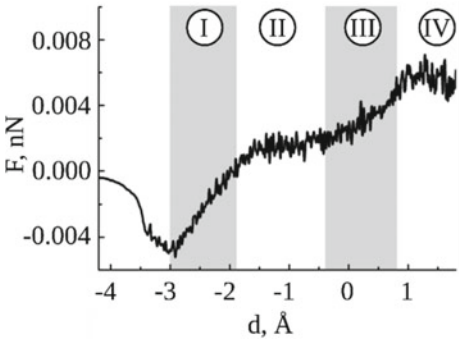


**Fig. 9** Dependence of the loading force on the indentation depth

in an ideal crystallite leads to a partial relaxation of excess stresses and a decrease in the slope of the curve with its subsequent transition to plateau in Fig. 9. The change in the behavior of the loading force during the transition from the first stage to the second is also associated with the discreteness of the indenter structure. In particular, during the indenter penetration, new atomic layers of the indenter start to interact with the free surface of the crystallite. The number of defects in the contact zone at the second stage quickly reaches saturation, and their number at the third stage changes insignificantly. This is due to the fact that the mechanism of excess stress relaxation by the generation of structural defects exhausts itself, resulting in an increase in the slope of the loading curve. An analysis of the simulation results shows that further indenter penetration (the beginning of the fourth stage) leads to an intensive increase in the number of local structural transformations. This leads not only to a slowdown in the growth of the loading force but to its superseeding by a decrease. Moreover, local structural transformations lead to the nucleation and development of structural defects of a higher rank, in particular, intrinsic and extrinsic stacking faults (SFs) (Fig. 10b). Structural defects in the contact zone are generated in the {111} atomic planes. Formed defects can spread along the indicated planes to the free surfaces. Their escape to the free surface leads to the formation of steps that change the crystallite shape. The defect structure in the loaded crystallite at the moment of the SF escape to the free surface is shown in Fig. 10c. The step on the free surface can be seen in Fig. 10d.

Note that the crystallite structure, its crystallographic orientation, indenter shape, loading scheme, and boundary conditions have a significant effect on the simulation results. To study the effect of the orientation of the loaded surface on the response of the material during indentation, the calculations were carried out for three surfaces with small Miller indices: $(01\bar{1})$, (001) and (111). The simulated samples had the shape of a cube with a side of 165 Å and consisted of 350,000 atoms. The loading scheme was similar to that described earlier, except that periodic boundary conditions were set along the axis of the cylindrical indenter. The indentation speed was 50 m/s. The influence of the orientation of the loaded surface on the formation of structural defects was studied based on the calculation of the dependences of the indentation

force $F(d)$ and the fraction of atoms $n$ involved in local structural changes on the indentation depth $d$ (Fig. 9).

The calculation results of the $F(d)$ and $n(d)$ curves for the $(01\bar{1})$ orientation of the loaded surface are shown in Fig. 11. Marks on the $F(d)$ curve indicate the indentation depths at which the loading curve abruptly changes the angle of inclination or has pronounced kinks. Projections of the crystallite structure for indentation depths corresponding to these points are shown in Fig. 12. We found that the features of the $F(d)$ and $n(d)$ curves correlate well with each other. In particular, the calculations show that the local structural changes lead to a decrease in the slope of the indentation force curve or to the appearance of an extremum in the loading curve due to relaxation of internal stresses.

Initially, an attractive force begins to act on indenter as it approaches the sample (the region of negative values in Fig. 11), and reaches its absolute maximum at a distance of 3.0 Å from the loaded surface. This "dip" in the curve of the loading force is accompanied by a bending of the loaded surface towards the indenter.

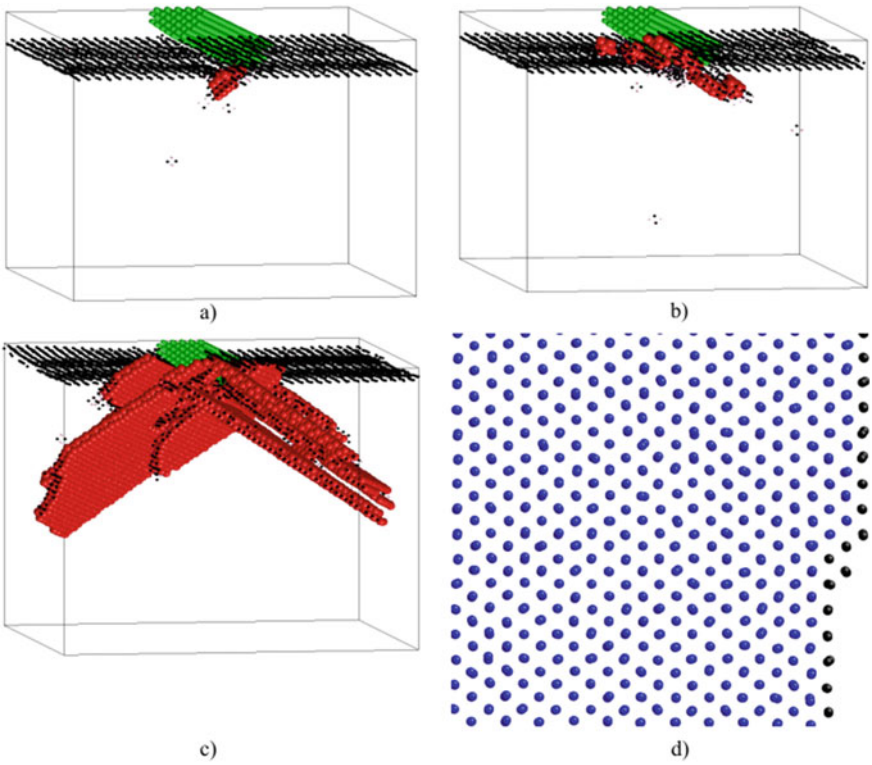


**Fig. 10** Fragment of the simulated crystallite for indentation depths: **a** −1.0 Å, **b** 1.5 Å, **c** 8.7 Å. Atoms with the fcc symmetry of the nearest environment are not shown. Green spheres indicate indenter atoms, red large spheres, and dark points indicate atoms with hcp and undefined symmetry of the nearest environment, correspondingly. **d** a step on the free surface

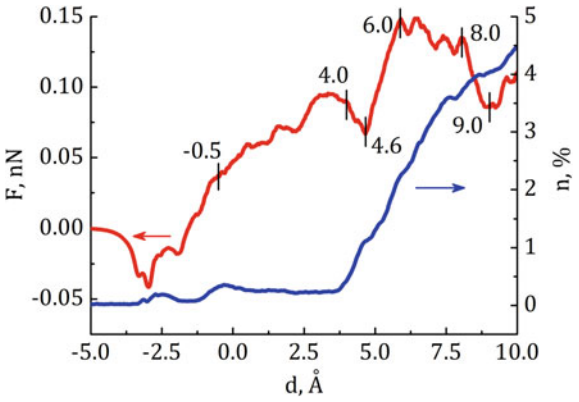


**Fig. 11** Dependences of the loading force (red curve) and the fraction of atoms involved in local structural changes (blue curve), on the indentation depth in the sample with the (01 $\bar{1}$) loaded surface

A change in the shape of the loaded surface leads to the generation of local structural changes in the region under the indenter. An analysis of the structure showed that the atoms in this region have 12 nearest neighbors, but their environment does not correspond to any of the known lattices. With further indentation, the surface returns to its previous position, the number of defects decreases, and the loading force remains practically unchanged when the indenter moves in the range from −2.5 to −1.8 Å. Then the loading force begins to grow with a constant number of defects. After passing the depth of −0.5 Å, its slope decreases. This is due to an increase in the number of local structural changes that form a/6 < 112 > {111} partial dislocations, and then SFs. They are located in adjacent (11$\bar{1}$) and (1$\bar{1}$1) planes (Fig. 12a). Further, the number of local structural changes slightly decreases. In this case, dislocations remain motionless, which leads to a further increase in the loading force.

Starting from an indentation depth of 3.6 Å, new SFs are generated and grow in the crystallite. They are located in the area under the indenter in planes of the same type, but deeper than previously formed SFs. The latter also begin to increase in size (Fig. 12b). In this case, a significant decrease in the loading force is observed, which continues until the indenter depth reaches 4.6 Å. The number of defects continues to increase at further loading, but the loading force begins to grow. This is due to the fact that the trailing partial dislocations move from the contact zone towards the free surface (Fig. 12c, d). At an indentation depth of 6.0 Å, the maximum value of the loading force is reached. The escape of dislocations to free surfaces leads to change of the shape of the crystallite, in particular, to the formation of steps on the free surface (Fig. 12e, f).

The simulation results of the copper crystallite behavior upon indentation of the (001) free surface are shown in Fig. 13. The peculiarities of the loading force curve in this figure correlate well with the peculiarities of the curve describing the number of atoms involved in local structural changes.

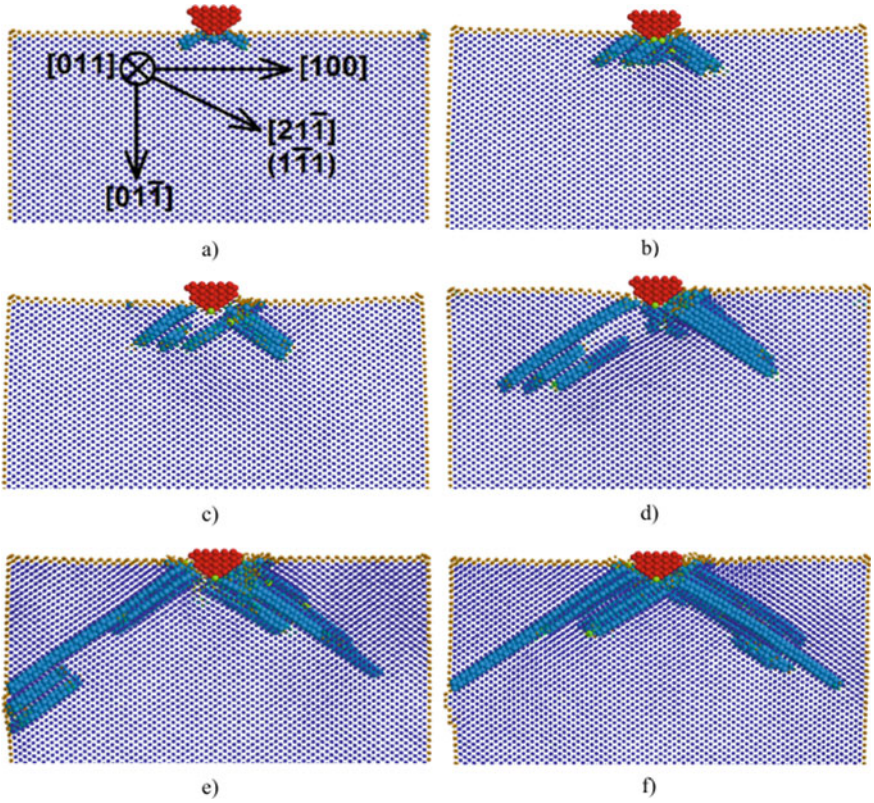


**Fig. 12** Fragment of the crystallite structure with the (01 $\bar{1}$) loaded surface at different indentation depths: **a** −0.5 Å, **b** 4.0 Å, **c** 4.6 Å, **d** 6.0 Å, **e** 8.0 Å, **f** 9.0 Å. Large blue and green spheres show the atoms with hcp and undefined symmetry of the nearest environment, respectively. Indenter atoms are marked in red

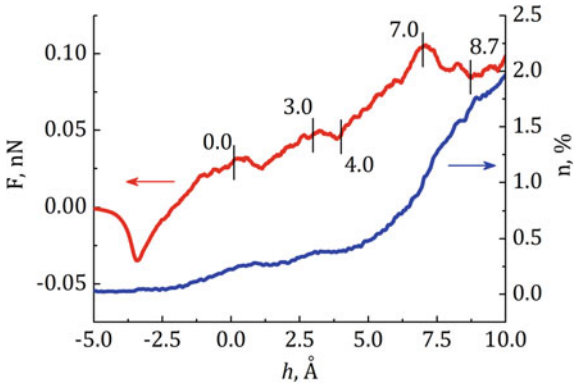


**Fig. 13** Dependences of the loading force (red curve) and the fraction of atoms involved in local structural changes (blue curve) on the indentation depth in the sample with the (001) loaded surface

The attractive force of the indenter to the surface reaches its maximum value at a distance of -3.4 Å. The number of defects increases due to the bending of the free surface. At further indentation, the loading force and the number of atoms involved in local structural changes begin to grow. Note that the curve of the loading force has features at the indentation depths of 0 and 3 Å. They are related to the discrete structure of the indenter. As the indenter penetrates the material, the atomic rows of the indenter alternately interact with the crystallite. Since distant atomic rows are initially attracted to the loaded surface, this leads to a slowdown in the growth of the loading force.

An analysis of the structure of the simulated crystallite showed that at the indentation depth of 0.8 Å, a region containing atoms with either hcp or undefined symmetry of the nearest environment is formed in the contact zone (Fig. 14a). The sizes of this region are comparable with the sizes of the indenter. With further indentation, the width of the region along the [010] direction doubles and then does not change. At the same time, the size of the defective region along the [001] direction increases with the penetration depth of the indenter. Note that a more intensive increase in the density of defects leads to a decrease in the loading force of the sample at an indentation depth of 7.0 Å.

Due to the inertia of accommodation processes, structural changes in the crystallite continue for some time after the indenter stops. During relaxation after the indenter stops at a depth of 10.0 Å, dislocation loops continue to move from the top of the region containing defects to the side free surfaces of the sample (Fig. 14c–e). The defect escape on free surfaces leads to the formation of steps (Fig. 14f), and the fraction of local structural changes decreases from 2.0 to 0.3%.

The simulation results of the copper crystallite behavior under indentation of the (111) free surface are shown in Fig. 15. The curves presented in this figure correlate quite well with each other.

Calculations showed that local structural changes begin to form in the sample at the indentation depth of −1.7 Å (Fig. 16a). Their formation slows down the growth of the loading force. The SF starts to grow in the $(11\bar{1})$ free surface at the indentation depth of 0.8 Å (Fig. 16b), and the loading force changes slightly.

The leading and trailing $a/6 < 112 > \{111\}$ partial dislocations are generated and move in adjacent $(11\bar{1})$ planes during loading of the crystallite (Fig. 16c–e). As a result of this process, a twin is formed in the crystallite. Atoms with hcp symmetry of the nearest environment are located on its boundaries (Fig. 16f). Note the formation of a fragmented region in the contact zone. This region consists of hcp atoms and grows towards the right side free surface (Fig. 16e, f).

In the case of bcc iron, the indenter was modeled by a repulsive force field in the form of a cylinder. The use of such an indenter reduces the effect of the structure discreteness on the structural response of the material. The sample dimensions with an ideal structure were 170 × 170 × 170 Å (Fig. 17a), and the dimensions of sample the with a GB was 230 × 170 × 170 Å (Fig. 17b). The projection of the structure of the $\Sigma 13$ (320)[001] symmetric tilt GB is shown in Fig. 18. The axis of the cylindrical indenter was oriented parallel to the loaded surface of the crystallites. The indenter force field was described by the formula: where $R$ is the indenter radius, $r$ is the

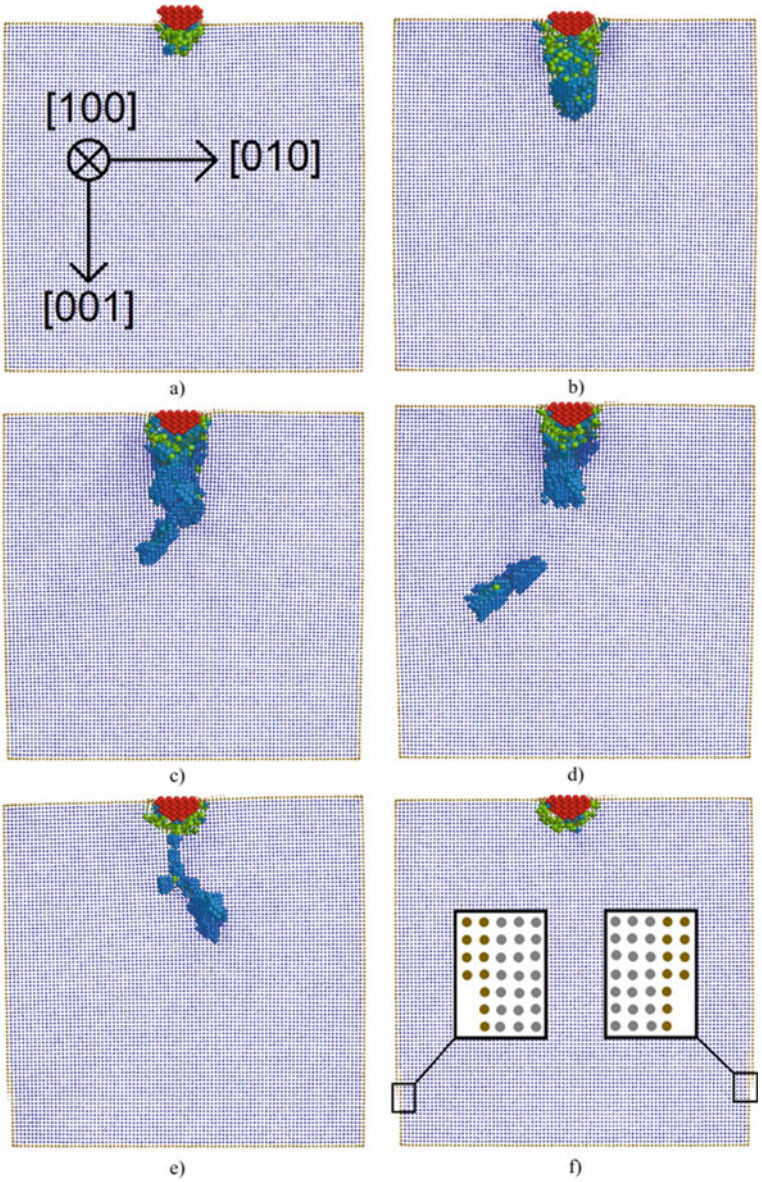


**Fig. 14** Crystallite structure under indentation of the (001) free surface at different indentation depths: **a** 4.0 Å, **b** 8.7 Å. The crystallite structure at different points in time after the indenter was stopped at the depth of 10 Å: **c** 40 ps, **d** 60 ps, **e** 80 ps, **f** 120 ps. Large blue and green spheres show the atoms with hcp and undefined symmetry of the nearest environment, respectively. Indenter atoms are marked in red

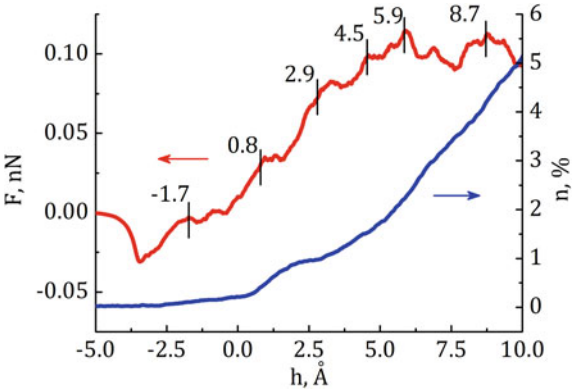


**Fig. 15** Dependences of the loading force (red curve) and the fraction of atoms involved in local structural changes (blue curve), on the indentation depth in the sample with the (111) loaded surface

distance from the indenter axis to the atom. The loading scheme was similar to that described previously for fcc samples of different orientations. The indenter was pressed in at a constant speed of 1 m/s. The kinetic temperature of the samples was 300 K.

$$U = \begin{cases} -\frac{(R-r)^4}{4}, & r < R \\ 0, & r > R \end{cases},$$

The dependences of the loading force on the indentation depth are shown in Fig. 19. The loading force curves for both crystallites are similar. The regions of linear growth of the loading force correspond to the elastic response of crystallites. The onset of plastic deformation (the formation of local structural changes) can be determined by an abrupt decrease in the loading force. An analysis of the indentation results showed that atoms involved in local structural changes have the value of the reduced slip vector exceeding 0.2. Note that, for a crystallite with the GB, plastic deformation nucleates at smaller indentation depths. Such a response is associated not only with the GB presence in the crystallite but also with the fact that the indenter contact line is oriented differently with respect to the loaded surface than in the case of a crystallite with an ideal lattice. The growth and drop of the loading force in Fig. 19 correlate well with curves showing a change in the number of atoms forming local structural changes.

An analysis of the simulation results shows that local structural changes initially nucleate in the region of contact of the indenter with the surface, and then propagate along the slip planes towards the lateral faces of the crystallite (Fig. 20). Their escape to the side face leads to the formation of a step on the free surface. Note that the GB prevents the propagation of local structural changes in the neighboring grain, which is clearly seen in Fig. 20b.

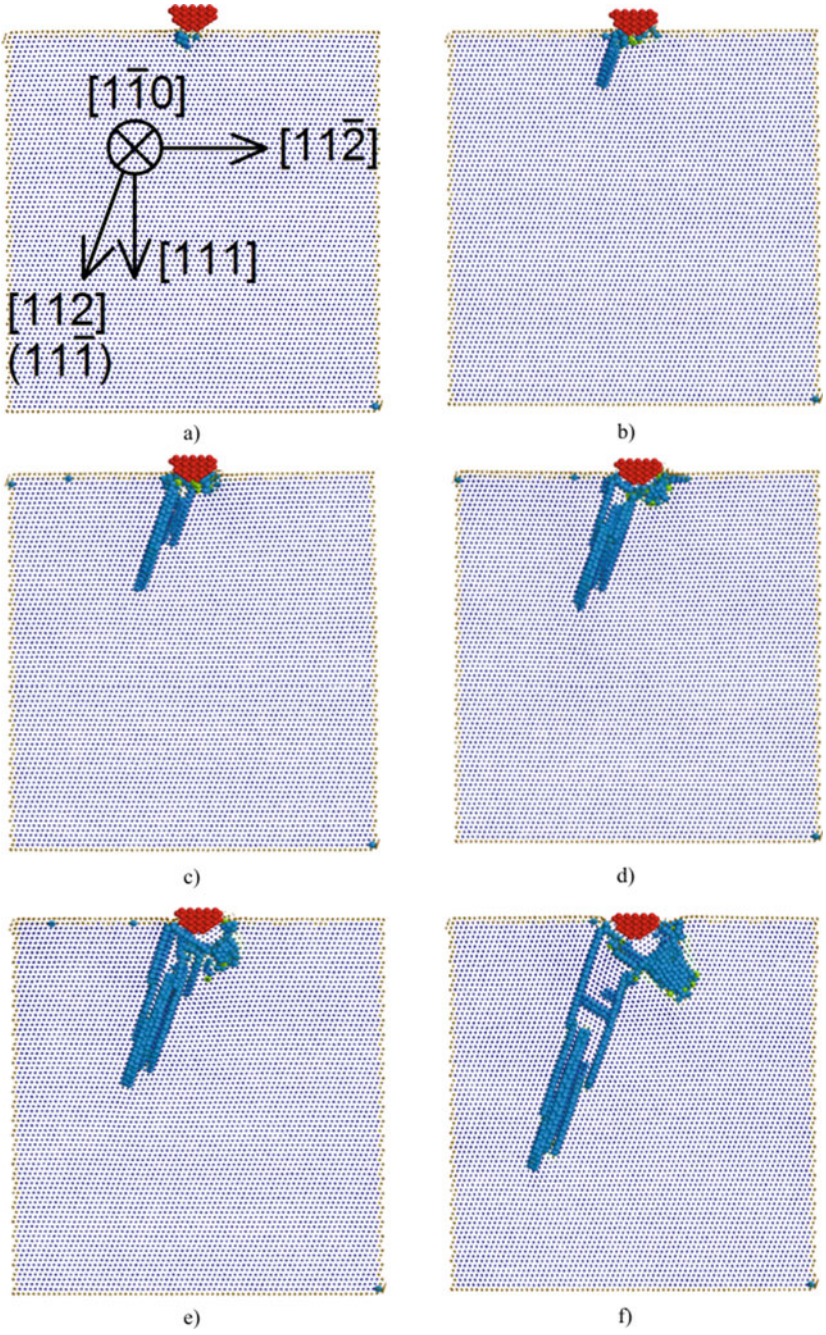


**Fig. 16** Crystallite structure under indentation of the (111) free surface at different indentation depths: **a** −1.7 Å, **b** 0.8 Å, **c** 2.9 Å, **d** 4.5 Å, **e** 5.9 Å, **f** 8.7 Å. Large blue and green spheres show atoms with hcp and undefined symmetry of the nearest environment, respectively. Indenter atoms are marked in red

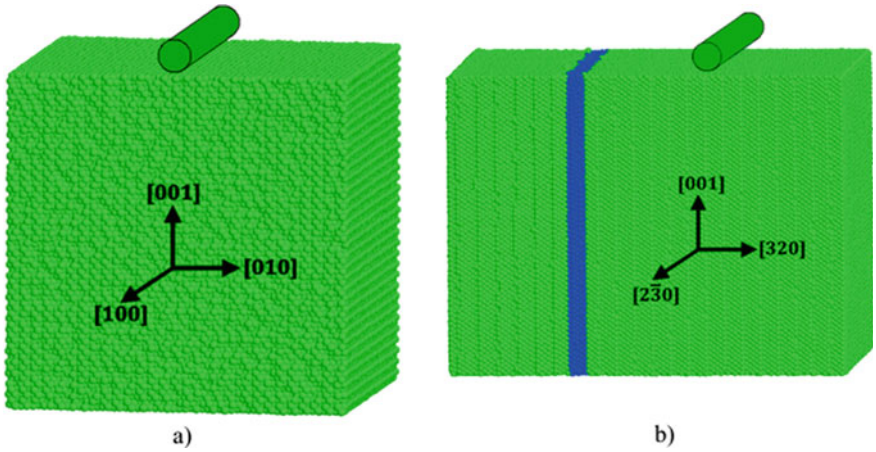


**Fig. 17** Scheme of loading for the sample with an ideal lattice (**a**) and with the GB (**b**). The GB region is marked in blue

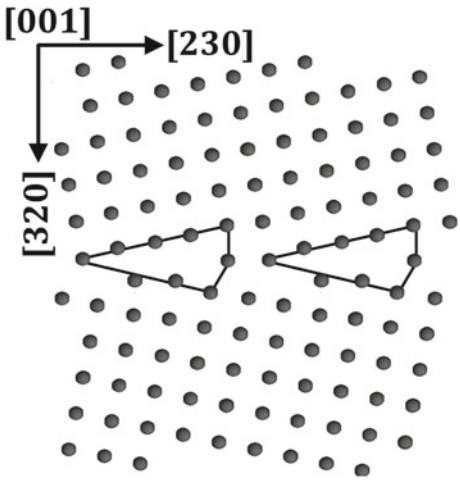


**Fig. 18** Projection of the Σ13 (320)[001] symmetric tilt GB structure onto the (001) plane after relaxation. Solid lines indicate GB structural elements

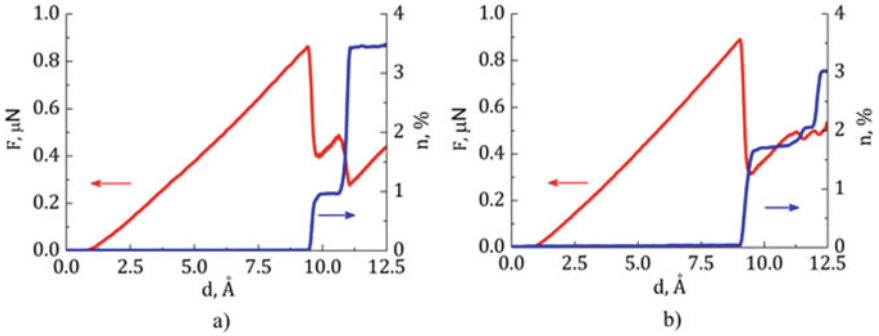


**Fig. 19** Loading force ($F$) and the fraction of structural defects ($n$) depending on the indentation depth ($d$) for the single crystal (**a**) and the sample with the GB (**b**)

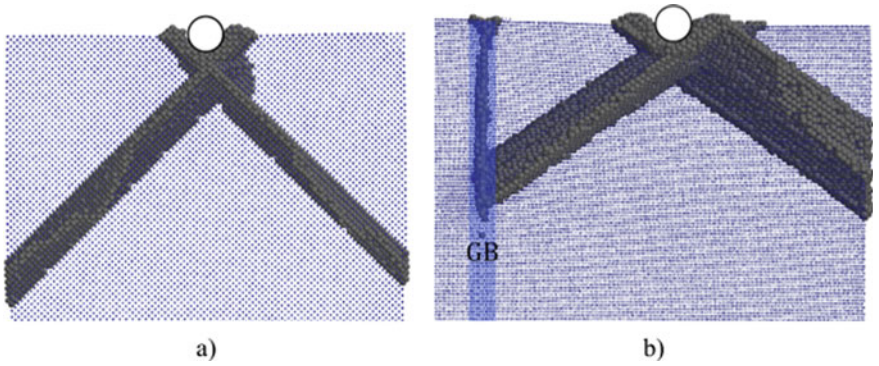


**Fig. 20** Projections of the sample structure with an ideal structure (**a**) and with the GB (**b**) for an indentation depth of 12.5 Å. Dark gray spheres show atoms which reduced slip vector is greater than 0.2

**Acknowledgements** The work was performed according to the Government research assignment for ISPMS SB RAS, project No. III.23.1.4.

## References

1. Panin VE, Pinchuk VG, Korotkevich SV, Panin SV (2017) Multiscaling of lattice curvature on friction surfaces of metallic materials as a basis of their wear mechanism. Phys Mesomech 20:69–77. https://doi.org/10.1134/S1029959917010064
2. Popov VL (2016) What does friction really depend on? Robust governing parameters in contact mechanics and friction. Phys Mesomech 19:115–122. https://doi.org/10.1134/S1029959916020016
3. Zolnikov KP, Korchuganov AV, Kryzhevich DS, Psakhie SG (2018) Dynamics of the formation and propagation of nanobands with elastic lattice distortion in nickel crystallites. Phys

Mesomech 21:492–497. https://doi.org/10.1134/S1029959918060036
4. Dmitriev AI, Nikonov AY, Shugurov AR, Panin AV (2019) The role of grain boundaries in rotational deformation in polycrystalline titanium under scratch testing. Phys Mesomech 22:365–374. https://doi.org/10.1134/S1029959919050035
5. Yan J, Lindo A, Schwaiger R, Hodge AM (2019) Sliding wear behavior of fully nanotwinned Cu alloys. Friction 7:260–267. https://doi.org/10.1007/s40544-018-0220-z
6. Ovid'ko IA (2007) Review on the fracture processes in nanocrystalline materials. J Mater Sci 42:1694–1708. https://doi.org/10.1007/s10853-006-0968-9
7. Korchuganov AV, Tyumentsev AN, Zolnikov KP, Litovchenko IY, Kryzhevich DS, Gutmanas E, Li S, Wang Z, Psakhie SG (2019) Nucleation of dislocations and twins in fcc nanocrystals: Dynamics of structural transformations. J Mater Sci Technol 35:201–206. https://doi.org/10.1016/j.jmst.2018.09.025
8. Wolf D, Yamakov V, Phillpot SR, Mukherjee A, Gleiter H (2005) Deformation of nanocrystalline materials by molecular-dynamics simulation: Relationship to experiments? Acta Mater 53:1–40. https://doi.org/10.1016/j.actamat.2004.08.045
9. Naik SN, Walley SM (2020) The Hall-Petch and inverse Hall-Petch relations and the hardness of nanocrystalline metals. J Mater Sci 55:2661–2681. https://doi.org/10.1007/s10853-019-04160-w
10. Koch CC (2007) Structural nanocrystalline materials: an overview. J Mater Sci 42:1403–1414. https://doi.org/10.1007/s10853-006-0609-3
11. Wu XL, Zhu YT (2008) Inverse grain-size effect on twinning in nanocrystalline Ni. Phys Rev Lett 101:025503. https://doi.org/10.1103/PhysRevLett.101.025503
12. Zhu YT, Wu XL, Liao XZ, Narayan J, Mathaudhu SN, Kecskés LJ (2009) Twinning partial multiplication at grain boundary in nanocrystalline fcc metals. Appl Phys Lett 95:031909. https://doi.org/10.1063/1.3187539
13. Monk J, Hyde B, Farkas D (2006) The role of partial grain boundary dislocations in grain boundary sliding and coupled grain boundary motion. J Mater Sci 41:7741–7746. https://doi.org/10.1007/s10853-006-0552-3
14. Kou Z, Yang Y, Yang L, Huang B, Luo X (2018) Twinning-assisted void initiation and crack evolution in Cu thin film: an in situ TEM and molecular dynamics study. Mater Sci Eng, a 737:336–340. https://doi.org/10.1016/j.msea.2018.09.069
15. Ovid'ko IA, Sheinerman AG (2006) Nanovoid generation due to intergrain sliding in nanocrystalline materials. Philos Mag a 86:3487–3502. https://doi.org/10.1080/14786430600643290
16. Ovid'ko IA, Valiev RZ, Zhu YT (2018) Review on superior strength and enhanced ductility of metallic nanomaterials. Prog Mater Sci 94:462–540. https://doi.org/10.1016/J.PMATSCI.2018.02.002
17. Psakhie SG, Zolnikov KP, Dmitriev AI, Smolin AY, Shilko EV (2014) Dynamic vortex defects in deformed material. Phys Mesomech 17:15–22. https://doi.org/10.1134/S1029959914010020
18. Cahn JW, Mishin Y, Suzuki A (2006) Coupling grain boundary motion to shear deformation. Acta Mater 54:4953–4975. https://doi.org/10.1016/j.actamat.2006.08.004
19. Psakh'e SG, Zol'nikov KP (1997) Anomalously high rate of grain boundary displacement under fast shear loading. Tech Phys Lett 23:555–556. https://doi.org/10.1134/1.1261742
20. Psakh'e SG, Zol'nikov KP (1998) Possibility of a vortex mechanism of displacement of the grain boundaries under high-rate shear loading. Combust Explosion Shock Waves 34:366–368. https://doi.org/10.1007/BF02672735
21. Plimpton S (1995) Fast parallel algorithms for short-range molecular dynamics. J Comput Phys 117:1–19. https://doi.org/10.1006/jcph.1995.1039
22. Mendelev MI, Han S, Son WJ, Ackland GJ, Srolovitz DJ (2007) Simulation of the interaction between Fe impurities and point defects in V. Phys Rev B 76:214105. https://doi.org/10.1103/PhysRevB.76.214105
23. Mendelev MI, Han S, Srolovitz DJ, Ackland GJ, Sun DY, Asta M (2003) Development of new interatomic potentials appropriate for crystalline and liquid iron. Phil Mag 83:3977–3994. https://doi.org/10.1080/14786430310001613264

24. Mishin Y, Farkas D, Mehl MJ, Papaconstantopoulos DA (1999) Interatomic potentials for monoatomic metals from experimental data and ab initio calculations. Phys Rev 59:3393–3407. https://doi.org/10.1103/PhysRevB.59.3393
25. Mendelev MI, King AH (2013) The interactions of self-interstitials with twin boundaries. Phil Mag 93(10–12):1268–1278. https://doi.org/10.1080/14786435.2012.747012
26. Mishin Y, Farkas D (1998) Atomistic simulation of [001] symmetrical tilt grain boundaries in NiAl. Philos Mag a 78(1):29–56. https://doi.org/10.1080/014186198253679
27. Stukowski A (2010) Visualization and analysis of atomistic simulation data with OVITO-the Open Visualization Tool. Modell Simul Mater Sci Eng 18(1):015012. https://doi.org/10.1088/0965-0393/18/1/015012
28. Zimmerman JA, Kelchner CL, Klein PA, Hamilton JC, Foiles SM (2001) Surface step effects on nanoindentation. Phys Rev Lett 87(16):165507. https://doi.org/10.1103/PhysRevLett.87.165507
29. Honeycutt JD, Andersen HC (1987) Molecular dynamics study of melting and freezing of small Lennard-Jones clusters. J Phys Chem 91:4950–4963. https://doi.org/10.1021/j100303a014
30. Rupert TJ, Gianola DS, Gan Y, Hemker KJ (2009) Experimental observations of stress-driven grain boundary migration. Science 326:1686–1690. https://doi.org/10.1126/science.1178226
31. Wen W, Becker AA, Sun W (2017) Determination of material properties of thin films and coatings using indentation tests: a review. J Mater Sci 52:12553–12573. https://doi.org/10.1007/s10853-017-1348-3
32. Ruestes CJ, Alhafez IA, Urbassek HM (2017) Atomistic studies of nanoindentation—a review of recent advances. Crystals 7(10):293. https://doi.org/10.3390/cryst7100293
33. Voyiadjis GZ, Yaghoobi M (2017) Review of nanoindentation size effect: Experiments and atomistic simulation. Crystals 7(10):321. https://doi.org/10.3390/cryst7100321
34. Gouldstone A, Chollacoop N, Dao M, Li J, Minor AM, Shen YL (2007) Indentation across size scales and disciplines: recent developments in experimentation and modeling. Acta Mater 55(12):4015–4039. https://doi.org/10.1016/j.actamat.2006.08.044
35. Psakhie SG, Zolnikov KP, Kryzhevich DS, Korchuganov AV (2019) Key role of excess atomic volume in structural rearrangements at the front of moving partial dislocations in copper nanocrystals. Sci Rep 9(1):3867. https://doi.org/10.1038/s41598-019-40409-9
36. Zeng FL, Sun Y, Liu YZ, Zhou Y (2012) Multiscale simulations of wedged nanoindentation on nickel. Comput Mater Sci 62:47–54. https://doi.org/10.1016/j.commatsci.2012.05.011
37. Hu X, Ni Y (2017) The effect of the vertex angles of wedged indenters on deformation during nanoindentation. Crystals 7(12):380. https://doi.org/10.3390/cryst7120380
38. Khajehvand M, Sepehrband P (2018) The effect of crystallographic misorientation and interfacial separation on jump-to-contact behavior and defect generation in aluminum. Mod Simul Mater Sci Eng 26(5):055007. https://doi.org/10.1088/1361-651X/aac427